Transit timing variation analysis of the low-mass brown dwarf KELT-1 b

Ö. Baştürk[1]⋆, J. Southworth[2], S. Yalçınkaya[1], L. Mancini[3,4,5], E. M. Esmer[1], M. Tekin[6],
F. Tezcan[7], D. F. Evans[2], C. T. Tezcan[7,8], I. Bruni[9], and C. Yeşilyaprak[7,8]

[1] *Ankara University, Faculty of Science, Astronomy & Space Sciences Department, Tandoğan, TR-06100, Ankara, Türkiye*
[2] *Astrophysics Group, Keele University, Staffordshire, ST5 5BG, UK*
[3] *Department of Physics, University of Rome "Tor Vergata", Via della Ricerca Scientifica 1, I-00133, Rome, Italy*
[4] *Max Planck Institute for Astronomy, Königstuhl 17, D-69117, Heidelberg, Germany*
[5] *INAF – Osservatorio Astrofisico di Torino, via Osservatorio 20, I-10025, Pino Torinese, Italy*
[6] *Middle East Technical University, Faculty of Science, Physics Department, Üniversiteler mah, TR-06800, Ankara, Türkiye*
[7] *Atatürk University, Science Faculty, Department of Astronomy and Space Sciences, 25240, Erzurum, Türkiye*
[8] *Atatürk University Astrophysics Research and Application Center (ATASAM), Yakutiye, 25240, Erzurum, Türkiye*
[9] *INAF – OAS, Osservatorio di Astrofisica e Scienza dello Spazio di Bologna, Via P. Gobetti 93/3, 40129, Bologna, Italy*

ABSTRACT

We investigate whether there is a variation in the orbital period of the short-period brown dwarf-mass KELT-1 b, which is one of the best candidates to observe orbital decay. We obtain 19 high-precision transit light curves of the target using six different telescopes. We add all precise and complete transit light curves from open databases and the literature, as well as the available TESS observations from sectors 17 and 57, to form a transit timing variation (TTV) diagram spanning more than 10 years of observations. The analysis of the TTV diagram, however, is inconclusive in terms of a secular or periodic variation, hinting that the system might have synchronized. We update the transit ephemeris and determine an informative lower limit for the reduced tidal quality parameter of its host star of $Q'_\star > (8.5 \pm 3.9) \times 10^6$ assuming that the stellar rotation is not yet synchronised. Using our new photometric observations, published light curves, the TESS data, archival radial velocities and broadband magnitudes, we also update the measured parameters of the system. Our results are in good agreement with those found in previous analyses.

Key words: methods: data analysis - techniques: photometric - stars: fundamental parameters - stars: individual: KELT-1 - planetary systems.

1 INTRODUCTION

KELT-1 b was the first low-mass companion found by the Kilodegree Extremely Little Telescope-North survey (KELT-North) for transiting planets (Siverd et al. 2012). It is the closest known low-mass brown dwarf (BD) to its host star, orbiting every $P_{\rm orb} = 1.2175$ d. At such a small orbital separation, tidal effects will lead to the transfer of angular momentum between the planetary orbit and the stellar spin. If the rate of the stellar rotation is longer than the orbital period, which is the usual case for giant planets in short-period orbits around cool stars, then the orbit is expected to decay and the star to spin up (Ogilvie 2014). KELT-1 b, with its relatively large radius (~ 1.14 $R_{\rm Jup}$), high mass (~ 27.7 $M_{\rm Jup}$), and short period, should experience strong tidal interactions with its host star, making it a good candidate for the detection of orbital decay. However, its mid-F host star (effective temperature $T_{\rm eff} \sim 6470$ K) should have a thin convective envelope, which will not be efficient in dissipating the energy produced by the tidal interactions with the BD companion. This low efficiency will have an important effect on the properties of the system. Therefore, it is dynamically interesting to study the observable consequences of tidal interactions.

A lower energy dissipation efficiency is expected from the host star compared to that for cooler stars with thicker convective envelopes, which could prolong its survival in the very short-period orbit where it currently exists. This raises a question about the tidal quality parameter, which quantifies the dissipation of the tidal energy ($Q'_\star$) by the host star. Siverd et al. (2012) found that for $Q'_\star = 10^8$, the orbital decay timescale should be less than 0.3 Gyr, which is shorter than the age of the system. Based on a canonical value of $Q'_\star = 10^6$ and the parameters of the system, the mid-transit time should shift by approximately 10 minutes after 10 years of observation with respect to a reference mid-transit time (Maciejewski et al. 2018). Baluev et al. (2015) analyzed the published transit light curves accumulated until the time of their study. They found no TTVs except for a tentative difference of 0.6 s in the orbital period, and corrected the linear ephemeris as a result. Maciejewski et al. (2018) also analyzed the published transit light curves in addition to their nine transit observations to reveal potential timing variations of the system. Although they did not find a statistically significant quadratic trend in the mid-transit times, they were able to constrain $Q'_\star$ to have a lower limit of 8.4×10^5 at 95% confidence based on the best fitting quadratic function, which is slightly lower than the canonical value they assumed (Barker & Ogilvie 2009). Maciejewski et al. (2022) recently strengthened this limit to $2.33^{+0.36}_{-0.38} \times 10^6$ based on new observa-

tions of KELT-1 from ground- and space-based facilities, including the Transiting Exoplanet Survey Satellite (TESS; Ricker et al. 2015) mission data from sector 17.

The projected rotational velocity of the host star (corresponding to 1.329 ± 0.060 d assuming spin-orbit alignment; Siverd et al. 2012) points to synchronization with the orbital motion, the timescale of which is also expected to be short. This finding is in agreement with a suggested value of the rotation period, $P_{rot} = 1.52 \pm 0.29$ d, from von Essen et al. (2021). The authors found this as a residual frequency in the periodogram of the TESS light curve pre-whitened for the ellipsoidal variation, reflection, and Doppler beaming effects. However, the relatively hot host star is not observed to be very active. It therefore does not have large enough surface inhomogeneities to produce prominent flux variations that surpass the dominant reflection effect and the ellipsoidal variation, which would have helped us determine the rotation period unambiguously. Nevertheless, the system can be argued to be synchronized due to tidal interactions with its host star. If tidal equilibrium has been achieved, then the orbital period should be stable. However, the slight difference between the rotational periods derived from spectroscopy and spot-induced variations can be important given the large uncertainties, indicating that the spin-up of the host star may not be complete and the system might not yet have reached tidal equilibrium.

KELT-1 b is also intriguing in terms of its mass and formation mechanism, which further complicate its classification. Because its mass of $27.7\,M_{Jup}$ exceeds the mass limit for deuterium burning (Spiegel et al. 2011), it is classified as a low-mass BD. However, it is in the so-called BD desert (Grether & Lineweaver 2006) which is a scarcity of BD-mass objects at short-period orbits compared to planetary and stellar-mass objects. In fact, its mass is very close to the intersection of the opposite-slope mass functions for planetary and stellar companions at short-period orbits at $\sim 30\,M_{Jup}$, where the desert is driest (Grether & Lineweaver 2006). The question is then whether it formed in the protoplanetary disk via the core accretion mechanism and migrated inwards, or formed directly by gravitational instability at a greater distance. Either case makes in-situ formation unlikely and increases the likelihood of a migration history. The M-dwarf companion to the KELT-1 system at $0''.5$ (150 au if it is bound) might have played a role in this history too (Siverd et al. 2012). *Gaia* DR3 measurements indicate a faint object with a mean *Gaia* magnitude of $G \sim 21$ at $7''.26$ separation with a large error bar due to its faintness. However, it is unlikely to be the object seen in the high angular resolution imaging because *Gaia* is unable to detect objects with a large contrast between them and within $2''$ of each other (Brandeker & Cataldi 2019; Mugrauer et al. 2022).

The circularization timescale is also short for KELT-1 b's orbit. However, *Spitzer* secondary eclipse observations (Beatty et al. 2014) are inconclusive in terms of orbital eccentricity. On the other hand, light curve solutions without the assumption of a circular orbit give a better fit for very small, but non-zero eccentricities (von Essen et al. 2021). A potential perturber at a larger orbital period might be the source of such an eccentricity.

The mass and short orbital period of KELT-1 b suggest that orbital decay should be observable on the timescale of a decade using data of typical quality from 1–2 m class ground-based telescopes (Birkby et al. 2014; Maciejewski et al. 2018). The presence of a potential perturber, a possible cause of the claimed non-zero eccentricity in the orbit of KELT-1 b, can also be investigated in the same data. While the former effect will lead to a secular change in the orbital period, the latter will cause periodic changes in the arrival times of the transit signals of the planet due to the reflex motion about the common centre of mass with the perturbing body, via the Light-Time Effect (LiTE). These arguments prompted us to observe the system regularly in order to investigate potential variations in the transit timings due to both possibilities. We observed 19 transits of KELT-1 b in total with different telescopes for ten years between 2012 and 2022. We also collected all the transit light curves from the Exoplanet Transit Database (ETD) and the literature, and downloaded the TESS 2-minute cadence light curves recorded during sectors 17 and 57 from the Mikulski Archive for Space Telescopes (MAST) web portal[1] of the Space Telescope Science Institute (STScI). We then analyzed all the light curves with EXOFAST (Eastman et al. 2013) and derived the mid-transit times to form a homogeneous dataset spanning more than ten years of observations for a thorough TTV analysis.

The paper is organised as follows. We present our observations and data reduction scheme in Section 2. The results of our analysis for the global modelling of the system, based on the most precise light curves, and for the transit timing are described in Section 3. The interpretation of the results is discussed in Section 4.

2 OBSERVATIONS AND DATA REDUCTION

We observed nine transits of KELT-1 b with the 1.23 m telescope at the Calar Alto Observatory (CAHA) in Spain. We used the telescope-defocusing method to obtain a high photometric precision (Southworth et al. 2009). The DLR-MKIII CCD camera gave a field of view (FoV) of $21' \times 21'.5$ at a plate scale of $0''.32$ per pixel. Six of the light curves were obtained through the I_c filter, two in R_c, and one in V.

Two transits were observed with the 1.52 m Cassini Telescope at the Astronomical Observatory of Bologna in Loiano (Italy) using a Gunn-i filter. The plate scale of the CCD was $0''.58$ per pixel, the FoV was $13' \times 12'.6$, and the telescope was defocused.

One transit was observed with the 64-megapixel Bonn University Simultaneous Camera (BUSCA) on the 2.2 m telescope at CAHA on 30 September 2016, simultaneously with the 1.23 m telescope. Observations were obtained simultaneously through four filters: Strömgren uby and Gunn-z. The data from the CAHA and Loiano observatories were reduced using the DEFOT code Southworth et al. (2014), which implements aperture photometry plus optimal weighting of comparison stars in the calculation of a differential-magnitude light curve. Unfortunately, the weather conditions were relatively poor so the ingress of the transit was not observed and the scatter in the remainder of the observations is higher than expected. The transit times measured from these data differ by almost 3 min from the light curve from the 1.23 m telescope so we did not include them in our TTV analysis. The light curve acquired during the same night using the 1.23 m telescope is also not included, because it was noisy and we have much more precise light curves in the R-band. However, we did include the Gunn-z data in the global modelling because it extends our wavelength coverage and the photometric precision is acceptable. The transit during the night of 12 September 2013 was also recorded simultaneously in these two observatories with Cousins-I (CAHA) and Gunn-i (Loiano) filters. We provide these light curves in Fig. 1 to illustrate the relative success of these observations in passbands with similar transmission functions.

We made use of the recently installed *Prof. Dr. Berahitdin Albayrak Telescope* (T80) at Ankara University Kreiken Observatory (AUKR) of Türkiye for four successful transit observations. The back-illuminated CCD with 1k pixels of 13 μm size provides a FoV of

---

[1] https://mast.stsci.edu/portal/Mashup/Clients/Mast/Portal.html
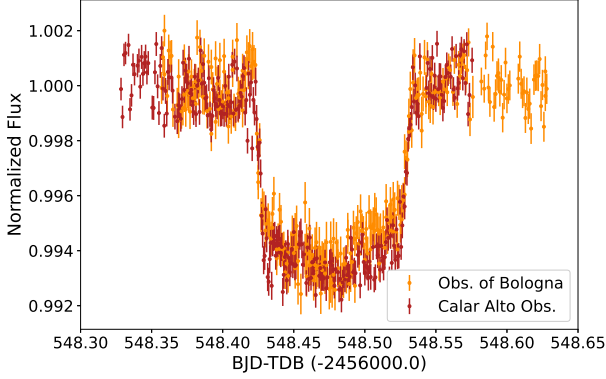
Figure 1. Normalized light curves recorded with the 1.52 m telescope in Observatory of Bologna in Loiano (in orange) and 1.23 m telescope in Calar Alto Observatory (in dark red) within Gunn *i* and Cousins-I, respectively on 12 September 2013.

$11'.84 \times 11'.84$ when used with a focal reducer that reduces the plate scale to $53''.4$ per mm operated at the back of the 80 cm primary mirror. We employed SDSS-*g′* (two nights), SDSS-*r′* (one night), and SDSS-*i′* (one night) filters during the observations.

We also observed a transit of KELT-1 b with the 1 m Turkish telescope T100, located at TÜBİTAK National Observatory of Türkiye (TUG) on the summit of Bakırlıtepe mountain (altitude 2500 m). The $f/10$ focal ratio provided a $21''$ mm^{-1} plate scale and an effective FoV of $21' \times 21'$. The readout from the 4096×4096 pixel CCD took 45 s in the unbinned mode, which we employed due to the brightness of the star, allowing a good sampling of the 2.5 hour-long transit, except for the ingress of the transit due to imperfect weather conditions just before the ingress. Therefore we had to exclude this light curve from the timing analysis. A Bessell *R*-band filter was used during the observation.

Finally, two transits of the target were observed with a Johnson-*R* filter with the 50 cm Ritchey-Chrétien (RC) telescope (ATA50) of the Atatürk University's ATASAM Observatory in Erzurum, Türkiye, located at an altitude of 1824 m. The Apogee Alta U230 CCD with 2048×2048 pixels, each of which has a size of $15\,\mu$ m, provides a pixel scale of $0.77''$ per pixel and an effective FoV of $13' \times 13'$. The data from the T80, T100 and ATA50 telescopes were reduced using the AstroImageJ (AIJ) (Collins et al. 2017) software package to obtain differential aperture photometry with respect to ensembles of comparison stars, yielding precise transit light curves for analysis in the current work. We used the observations from ATA50 and T80 only in the timing analysis, because we have more precise light curves in the same passbands which are more suitable for the global modelling.

KELT-1 was observed by TESS during sector 17 between 7 Oct 2019 and 2 Nov 2019, and sector 57 between 30 Sep 2022 and 29 Oct 2022. Both sectors were observed in short-cadence mode so have 2 min integration times. These data were obtained from the MAST Portal. We examined the Target Pixel Files (TPF), Simple Aperture Photometry (SAP) and Pre-search Data Conditioning SAP (PDC-SAP) light curves (Jenkins et al. 2016). We performed photometry with different apertures for both the target and the background, and compared our results with the SAP and PDCSAP light curves. Since von Essen et al. (2021) studied the out-of-transit variability and the secondary eclipse in detail, we concentrated on the transit profiles to derive their mid-transit timings. We decided to use the light curves

from the Data Validation Timeseries files (DVT), which are detrended from the correlated noise sources and hence stood out as the most convenient data type for our purpose. The visual companion at $\sim 0''.5$, found by Siverd et al. (2012) in high-resolution images, cannot be resolved in either TESS images or our own observations. It was found to be fainter by 5.6 mag in the *H*-band and 5.9 mag in the *K*-band so its flux contribution is less than 0.2% at the optical wavelengths covered by our observations. This is well below the limit at which its contribution to the light curve is important (Southworth et al. 2020).

We detrended some of our light curves that are affected by correlated noise. Instrumental effects, e.g. drifts in the x-y positions of stars on the CCD images due to imperfect telescope tracking and non-linearity issues, occasional clouds and other variability sources in weather conditions, all contribute to the red-noise budget for small (1 m diameter or less) telescopes. Although we have not observed any obvious signatures of surface inhomogeneities induced by stellar activity on the raw light curves, which would affect their morphologies and eclipse depths, potential light curve asymmetries due to spot-crossing events in the transit chord may have also been smoothed out from the light curves we detrended. This is not very likely because KELT-1 is a mid-F type star with no indication of strong activity other than the tentative periodicity reported by von Essen et al. (2021). We employed a quasi-periodic kernel function for the stochastic part of a Gaussian Process (GP) accounting for both systematics and potential stellar variability. The deterministic part of the GP was defined by the base transit model. The centre and width of the Gaussian priors of the parameters in the transit models were set to the values derived by Beatty et al. (2017). The orbit was assumed to be circular. We normalized the out-of-transit flux to 1 for all the transit light curves. We employed a normal distribution for the white noise, which we controlled carefully and preserved its standard deviation to remove only the red noise component as efficiently as possible. In this manner, we detrended some of our light curves from correlated noise as described in Yalçınkaya et al. (2021), which we denoted with a "d" in the observing log (Table 1). We quantified the white and red (correlated) noise levels in all the light curves with the widely-used Photon Noise Rate (PNR) (Fulton et al. 2011) and β-factor (Winn et al. 2008) parameters, respectively and presented them in Table 1.

3 ANALYSIS AND RESULTS

3.1 Global Modelling

We selected the "best" transit light curves of KELT-1 b, based on PNR and β-factor statistics, in different passbands to extend the wavelength coverage as much as possible for a global modelling to derive system and planetary parameters. Since we detrended some of our light curves, they have been corrected for spot-induced modulations, observational effects, and correlated noise due to instrumental effects and stellar variability. Because they have longer timescales than the transit duration, amplitudes far too small to be recovered by ground-based observations, and because we did not have a low-frequency component in the GP, the reflection effect, Doppler boosting, and ellipsoidal variations are already included in the white-noise budget. Although the detrended light curve in the SDSS-*r′* band acquired with T80 in Ankara is of high quality, there is a superior light curve in the same passband obtained in the University of Louisville Moore Observatory (ULMO) published in the discovery paper (Siverd et al. 2012), which we used in the global modelling instead. We made use of two light curves (from BUSCA in Gunn-*z* and T100 in Bessell *R*

Table 1. Log of our transit observations of the transiting brown dwarf KELT-1 b. Light curves denoted with the letter *d* are detrended from the correlated noise and * were not used in the timing analysis since the ingress was not constrained well.

Telescope	Start date UTC	Start time UTC	End time UTC	Filter	Exposure time (s)	Images Number	PNR ppt	β	Mid-Transit BJD_{TDB}	Error (d)
CAHA^d	2012-09-09	00:14:22	04:54:54	I_c	145	113	0.239	1.386	2456179.576852	0.000177
CAHA	2012-10-22	19:47:03	01:59:39	V	120	163	0.489	2.956	2456223.407010	0.000447
CAHA	2013-09-12	19:45:51	01:41:36	I_c	70	277	0.628	2.410	2456548.477686	0.000235
Loiano	2013-09-12	20:26:58	02:57:11	Gunn-i	85	309	0.678	2.500	2456548.477458	0.000255
CAHA	2014-10-20	19:17:12	02:41:52	I_c	60	373	0.756	2.114	2456951.468633	0.000276
CAHA	2015-08-20	00:04:13	04:33:41	I_c	60	225	0.751	1.556	2457254.624048	0.000303
CAHA	2016-09-30	20:18:03	03:01:04	R_c	45	339	0.749	2.075	2457662.484192	0.000205
BUSCA^{d,*}	2016-09-30	20:42:05	03:00:31	Gunn-z	150	122	0.330	3.005	2457662.484985	0.000526
Loiano^d	2017-01-08	17:16:43	19:23:53	Gunn-i	80	183	0.821	1.035	2457762.318983	0.000379
CAHA^d	2017-08-04	22:03:15	02:11:01	I_c	90	120	0.475	1.606	2457970.511467	0.000252
CAHA	2017-08-21	20:38:25	04:13:18	I_c	55	356	0.769	1.861	2457987.556687	0.000305
CAHA	2017-09-23	19:18:25	02:00:36	R_c	60	335	0.530	1.641	2458020.427127	0.000200
T100^{d,*}	2019-10-29	16:06:22	21:22:33	Bessell R	120	115	0.432	1.120	2458786.231872	0.000357
T80^d	2021-07-29	20:27:35	00:20:08	SDSS-g'	150	91	0.557	1.171	2459425.416140	0.000541
T80^d	2021-08-26	19:28:27	23:18:06	SDSS-g'	80	164	0.988	0.855	2459453.419241	0.000421
ATA50^d	2021-09-28	16:12:41	21:30:37	R	150	115	0.844	1.636	2459486.290677	0.000670
T80^d	2021-10-10	20:59:35	01:59:22	SDSS-r'	80	197	0.851	1.236	2459498.465202	0.000370
ATA50^d	2021-10-26	15:08:19	22:28:08	R	150	142	0.505	1.664	2459514.293822	0.000503
T80^d	2022-11-11	18:51:31	22:34:31	SDSS-i'	110	115	0.461	0.956	2459895.368370	0.000273

during the global modelling although we discarded them from the timing analysis because the ingress was not constrained well due to poorer weather conditions at the time. While, light curves are analyzed separately to measure their mid-transit times, heavily influenced by the contact times of a transit, they are modelled as an ensemble to derive fundamental parameters of the system.

We then collected broadband apparent magnitudes of the host star in different passbands used mostly in space-borne observations (see Table 2) to fit the spectral energy distribution (SED) of the host star (Fig. 2) in EXOFASTv2 by using the Modules for Experiments in Stellar Astrophysics (MESA) Isochrones and Stellar Tracks (MIST) bolometric correction grid (Choi et al. 2016). The stellar (T_{eff}, metallicity ([Fe/H]) and surface gravity ($\log g$) were adopted from the most detailed spectroscopic analysis of the host star (Siverd et al. 2012) while the distance was calculated from the *Gaia* EDR3 parallax (Gaia Collaboration et al. 2016, 2021a,b) with the offset given by Lindegren et al. (2021) and provided as a Gaussian prior during the SED fitting. The maximum value of the interstellar extinction (A_V) along the line of sight was limited to the value given by Schlegel et al. (1998). As a result, we obtained T_{eff} = 6491^{+45}_{-45} K, $T_{eff,SED}$ = 6400^{+64}_{-56} K, $R_\star$ = $1.499^{+0.034}_{-0.032}$ R$_\odot$ and $R_{\star,SED}$ = $1.542^{+0.011}_{-0.012}$ R$_\odot$ from the SED fitting. The values with the SED subscript comes purely from the SED analysis, i.e. without a Gaussian prior on T_{eff}. We provided the empirically derived stellar radius from the best-fitting SED model (with the T_{eff} prior implied) as a Gaussian prior during global modelling to increase the accuracy of the absolute parameters of the system. The value of the Gaussian prior width for $R_\star$ was set to 3.5% of its value as suggested by Tayar et al. (2020). We also provided the T_{eff} value given by Siverd et al. (2012) instead of our SED value because the T_{eff} measurement from high-resolution spectra should be superior to the SED analysis.

We then simultaneously modelled the transit light curves that we selected together with the archival radial velocity (RV) data (Siverd et al. 2012) and the phase-folded TESS sector-17 data, supported by the information from the stellar evolution models, to derive orbital and physical properties of the system in EXOFASTv2 (Eastman 2017; Eastman et al. 2019). T_{eff} and [Fe/H] values from high-resolution spectroscopy and $R_\star$ from the SED fitting were as-
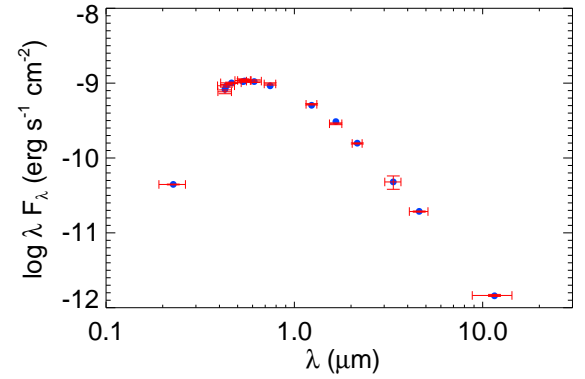
Figure 2. Broadband fluxes of KELT-1 (red data points with error bars) and model fluxes (blue points).

signed to the centres of the Gaussian priors. $\log g$ was most precisely constrained by the mean stellar density ($\rho_\star$) from the transit duration, via Kepler's third law, while TESS phase curve helps to better constrain the orbital eccentricity. All parameters apart from T_{eff}, [Fe/H] and $R_\star$ were assigned to uniform priors between $\pm\infty$. The initial values for these fundamental stellar parameters, on the other hand, were determined from our preliminary analysis by making use of the relations given by Torres et al. (2010), instead of using stellar evolutionary tracks, and we used only one light curve for each passband for speed in computation. The age and mass of the star ($M_\star$) were derived from the integrated MIST model, based on $\rho_\star$ and $R_\star$. The quadratic limb darkening coefficients were interpolated from the tables of Claret & Bloemen (2011) for each passband used in the observations, which were then set to the centres of uniform priors during the light curve modelling. Convergence is ensured for the parameters when independent chains of the MCMC run are found to be similar to each other, which is controlled by the Gelman-Rubin statistic (Rz), and the number of independent draws (Tz) being large enough so that the chains are sufficiently long compared to their cor-

Table 2. Broadband apparent magnitudes for KELT-1.

Passband	λ_{eff} (*nm*)	Magnitude
APASS-DR9 (Henden et al. 2016)		
Johnson B	437.81	11.189 ± 0.045
Johnson V	-	10.659 ± 0.045
SDSS g'	464.04	10.916 ± 0.022
SDSS r'	612.23	10.559 ± 0.044
SDSS i'	743.95	10.441 ± 0.038
GALEX (Bianchi et al. 2017)		
galNUV	227.44	15.089 ± 0.013
2MASS (Cutri et al. 2003)		
J_{2MASS}	1235	9.682 ± 0.022
H_{2MASS}	1662	9.534 ± 0.030
K_{2MASS}	2159	9.437 ± 0.019
All WISE (Cutri et al. 2021)		
WISE1	3352.6	9.414 ± 0.220
WISE2	4602.8	9.419 ± 0.020
WISE3	11560.8	9.386 ± 0.034
Tycho-2 (Høg et al. 2000)		
B_T	428.0	11.363 ± 0.065
V_T	534.0	10.701 ± 0.057

relation lengths (Eastman et al. 2019). Then the posterior distribution functions for the fit parameters are representative of the underlying posterior and the fit has converged. The computations stopped when converged, and a global model of the most precise transit light curves with a wide wavelength coverage, archival RV data, and broadband apparent magnitudes of the host was achieved. The values of the fit parameters are provided in Table 3, while the models for the light, phase and RV curves based on these parameter values are presented in Figs. 3, 4 and 5, respectively.

3.2 Transit timing analysis

In order to investigate a potential nonlinearity in the transit timings of KELT-1 b, we collected all the available transit light curves for the target in the Exoplanet Transit Database (ETD)[2], literature, and the TESS DVT light curves. We converted the mid-exposure timings of all data points to $\mathrm{BJD_{TDB}}$ if they were provided in a different time convention, based on the location of the telescope, the coordinates of the object and the reported timing, using the relevant modules in ASTROPY (Astropy Collaboration et al. 2013, 2018). We had to correct some of the light curves for linear trends primarily due to the effect of airmass.

In order to calculate mid-transit times from all of the available light curves, we used an approach that aims at homogeneity in the analysis. We derived the times of mid-transit from the EXOFAST transit models of all the light curves. We made use of the web-based version of the code through NASA Exoplanet Archive, which relies on the AMOEBA optimization algorithm. The transit parameters set as free and their initial values gathered from Siverd et al. (2012) This modelling choice significantly reduced the time spent in computations of the mid-transit times.

Although a probabilistic modelling scheme to derive the distributions for system parameters and their uncertainties would be optimal (EXOFASTV2), the accuracy and precision of the mid-transit timings from a fitting procedure based on an optimization algorithm (EXOFASTV1) are still reliable. We compared the mid-transit timings we measured using the web-based version of EXOFASTV1 to those from

Table 3. Median values and 68% confidence interval for KELT-1 b.

| Symbol	Parameter (Unit)	Values
Stellar parameters:		
$M_\star$	Mass ($M_\odot$)	$1.369^{+0.071}_{-0.075}$
$R_\star$	Radius ($R_\odot$)	1.501 ± 0.036
$L_\star$	Luminosity ($R_\odot$)	$3.56^{+0.22}_{-0.21}$
$\rho_\star$	Density (cgs)	$0.57^{+0.032}_{-0.028}$
$\log g$	Surface gravity (cgs)	$4.221^{+0.018}_{-0.017}$
T_{eff}	Effective Temperature (K)	6471^{+50}_{-49}
[Fe/H]	Metallicity (dex)	0.095 ± 0.080
$[\mathrm{Fe/H}]_0$	Initial Metallicity[1]	$0.211^{+0.066}_{-0.068}$
Age	Age (Gyr)	$1.65^{+0.89}_{-0.65}$
Planetary parameters:		
P_{orb}	Period (days)	$1.217493996(81)$
R_p	Radius (R_{jup})	1.138 ± 0.030
M_p	Mass (M_{jup})	$27.7^{+1.0}_{-1.1}$
a	Semi-major axis (au)	$0.02494^{+0.00042}_{-0.00046}$
i	Inclination (degrees)	$85.27^{+1.10}_{-0.85}$
e	Eccentricity	$0.0055^{+0.0084}_{-0.0039}$
$\omega_\star$	Argument of periastron (degrees)	-100^{+120}_{-130}
T_{eq}	Equilibrium temperature[6] (K)	2421 ± 28
τ_{circ}	Tidal circularization timescale (Gyr)	$0.133^{+0.015}_{-0.013}$
K	RV semi-amplitude (m/s)	4207 ± 57
$R_P/R_\star$	Radius of planet in stellar radii	$0.07792^{+0.00031}_{-0.00034}$
$a/R_\star$	Semi-major axis in stellar radii	$3.570^{+0.065}_{-0.061}$
δ	Fractional transit depth	$0.006072^{+0.000049}_{-0.000052}$
τ	Ingress/egress transit duration (days)	$0.00925^{+0.00035}_{-0.00036}$
T_{14}	Total transit duration (days)	0.11484 ± 0.00035
T_{FWHM}	FWHM transit duration (days)	0.10560 ± 0.00019
b	Transit impact parameter	$0.295^{+0.048}_{-0.064}$
τ_S	Ingress/egress eclipse duration (days)	$0.00920^{+0.00038}_{-0.00039}$
T_{14_S}	Total occultation duration (days)	$0.1146^{+0.0013}_{-0.0019}$
A_{ellips}	Ellipsoidal variation amplitude (ppm)	398 ± 19
δ_S	Measured eclipse depth (ppm)	388 ± 53
ρ_p	Density (cgs)	$23.3^{+1.6}_{-1.4}$
$\log g_p$	Surface gravity	$4.724^{+0.019}_{-0.018}$
Θ	Safronov number	$0.886^{+0.027}_{-0.025}$
Wavelength-dependent parameters:		
$u_{1,I}$	linear limb-darkening coeff in I	0.271 ± 0.016
$u_{2,I}$	quadratic limb-darkening coeff in I	0.352 ± 0.018
$u_{1,R}$	linear limb-darkening coeff in R	0.286 ± 0.025
$u_{2,R}$	quadratic limb-darkening coeff in R	0.337 ± 0.031
$u_{1,i'}$	linear limb-darkening coeff in i'	0.283 ± 0.033
$u_{2,i'}$	quadratic limb-darkening coeff in i'	0.346 ± 0.042
$u_{1,r'}$	linear limb-darkening coeff in r'	0.325 ± 0.035
$u_{2,r'}$	quadratic limb-darkening coeff in r'	0.342 ± 0.044
$u_{1,z'}$	linear limb-darkening coeff in z'	0.216 ± 0.043
$u_{2,z'}$	quadratic limb-darkening coeff in z'	0.336 ± 0.047
$u_{1,\mathrm{TESS}}$	linear limb-darkening coeff in TESS	0.179 ± 0.032
$u_{2,\mathrm{TESS}}$	quadratic limb-darkening coeff in TESS	0.257 ± 0.042
$u_{1,V}$	linear limb-darkening coeff in V	0.349 ± 0.037
$u_{2,V}$	quadratic limb-darkening coeff in V	0.312 ± 0.044

---

[2] http://var2.astro.cz/ETD/
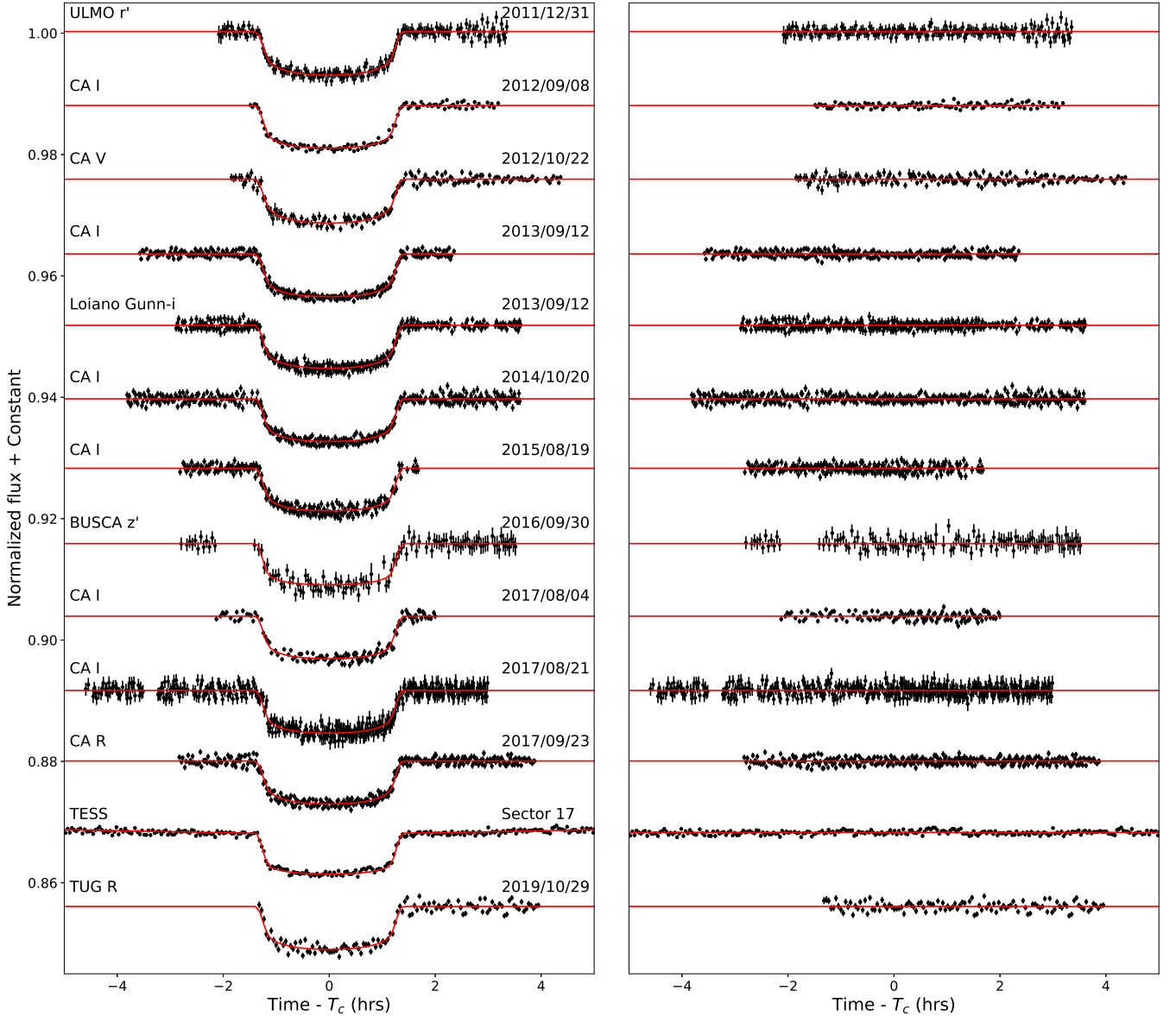
Figure 3. Our individual transit light curves and one light curve from Siverd et al. (2012) (on top) and their EXOFASTv2 models. Data points and their errorbars are in black, while their models are given with continuous red lines. CA: CAHA observations, TUG: TÜBİTAK National Observatory of Türkiye, BUSCA: Bonn University Simultaneous CAmera observations, ULMO: University of Louisville Moore Observatory. The residuals from the models are given in the right-hand panel.

our global modelling with EXOFASTv2, and found that the difference is less than 20 s and within 1.3 σ of all measurements having a minimum error bar of 15 s. This resulted in a homogeneously measured set of 72 mid-transit timings for KELT-1 b within a significantly reduced computation time.

In order to compute the timings expected from a linear ephemeris, we employed the orbital period (P_{orb}) value from Maciejewski et al. (2018) and the mid-transit time (T_0) we measured from the most precise light curve that we acquired with the 1.23 m telescope at CAHA on 20 August 2015 as reference elements. We then calculated the differences between these expected mid-transit timings based on a linear ephemeris (denoted as C for calculated from $C = T_0 + E \times P_{orb}$) and the actual observations of the timings of the conjunctions (denoted as O for observed) and plotted them with respect to the orbital cycle (epoch, E), and hence formed an O-C diagram. We had

to eliminate only two data points, both from the ETD, because they deviated in the diagram by more than 3σ of the mean O-C. These issues were very unlikely to be caused by an astrophysical mechanism that would lead to a sudden shift of these transits. This resulted in a total of 72 precise mid-transit times for analysis. A linear trend with a small slope was found due to the accumulation of uncertainties on the reference elements with time. We fitted a linear and a quadratic model to this dataset independently to update the linear ephemeris and search for a secular change in the orbital period, respectively.

We generated random samples for the fit parameters using a Markov Chain Monte Carlo (MCMC) algorithm based on 16 chains, 5000 iterations and a burn-in period to discard the first 500 steps, by making use of the relevant functions in the PyMC3 package (Salvatier et al. 2016) and calculated the likelihood of each sample based on its agreement with the TTV diagram. The posterior prob-
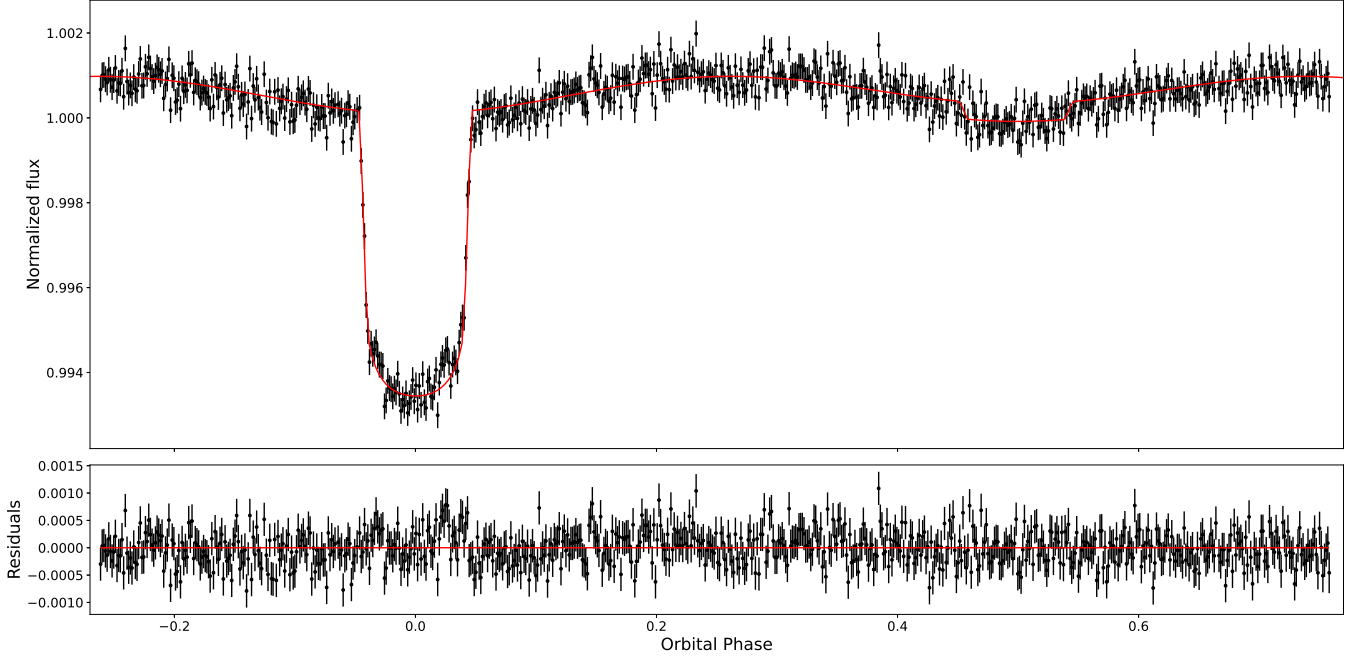
Figure 4. Phase folded TESS phase curve binned to 2 minutes from sector 17 (black points with error bars) and the best-fitting global model (red continuous line). Residuals are shown in the bottom panel.
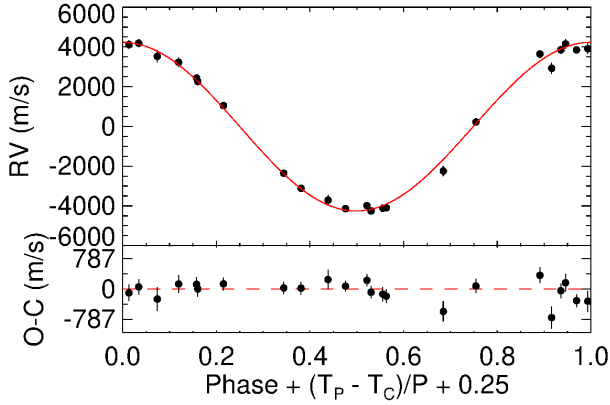
Figure 5. Archival RV observations from TrES (black data points) and the best-fitting Keplerian model (red continuous line). Residuals from the model are given in the bottom panel.

ability distribution of each fit parameter was computed, its median value was taken to be the value for the corresponding parameter, and the 16th and 84th percentiles were taken to be its uncertainty. The two parameters of the linear model were used to update the linear ephemeris as provided in Eq. 1.

$$T_0 = 2457254.624084(54) + 1.21749385(4) \times E \quad (1)$$

We followed the same procedure in fitting a quadratic function to investigate secular changes in the transit timings. We calculated the likelihoods of three coefficients of a parabola sampled from an MCMC run with the same hyper-parameters as we employed during the linear fit. We found a negative quadratic coefficient, in agreement

with the expected form of orbital decay. The quadratic ephemeris we found is:

$$T_0 = 2457254.624150(62) + 1.21749398(7) \times E$$
$$+ (-9.9 \pm 4.5) \; 10^{-11} \times E^2 \quad (2)$$

When we compare the fits, although the quadratic model performs slightly better than the linear in representing the data with a χ_ν^2 value of 2.273 compared to 2.308 for the latter, the values for Bayesian and Akaike Information Criteria (BIC and AIC) favour the linear model with ΔBIC and ΔAIC values of 4.24 and 1.96, respectively. Since the two-parameter linear model is simpler as well, there is no evidence for an orbital decay at the moment. Nevertheless, we provide both models and their uncertainties superimposed on O-C data in Fig. 6. Based on our updated ephemeris, we did not find any difference between the average mid-transit timings of two TESS sectors within the propagated uncertainties. This implies that there is no change on the orbital period over 2.9 year time interval covered by the TESS data within the limits of measurement uncertainties.

Since the linear model better fits the data, we are only able to place a lower limit on the reduced tidal quality factor. To do this we used the fifth percentile of the quadratic coefficient, A, to give an upper limit on the rate of change of period with observing epoch according to

$$A = \frac{1}{2} \frac{dP}{dE} \quad (3)$$

and converted this to a limit on $Q'_\star$ using the equation

$$Q'_\star = -\frac{27}{2} \pi \frac{M_P}{M_\star} \left(\frac{a}{R_\star} \right)^{-5} \left(\frac{dP}{dE} \right)^{-1} P_{\rm orb} \quad (4)$$

where the other parameters were taken from our global modelling results. Hence, assuming the system is not synchronized, we find $Q'_\star > (8.5 \pm 3.9) \times 10^6$ slightly larger than the canonical value of 10^6.
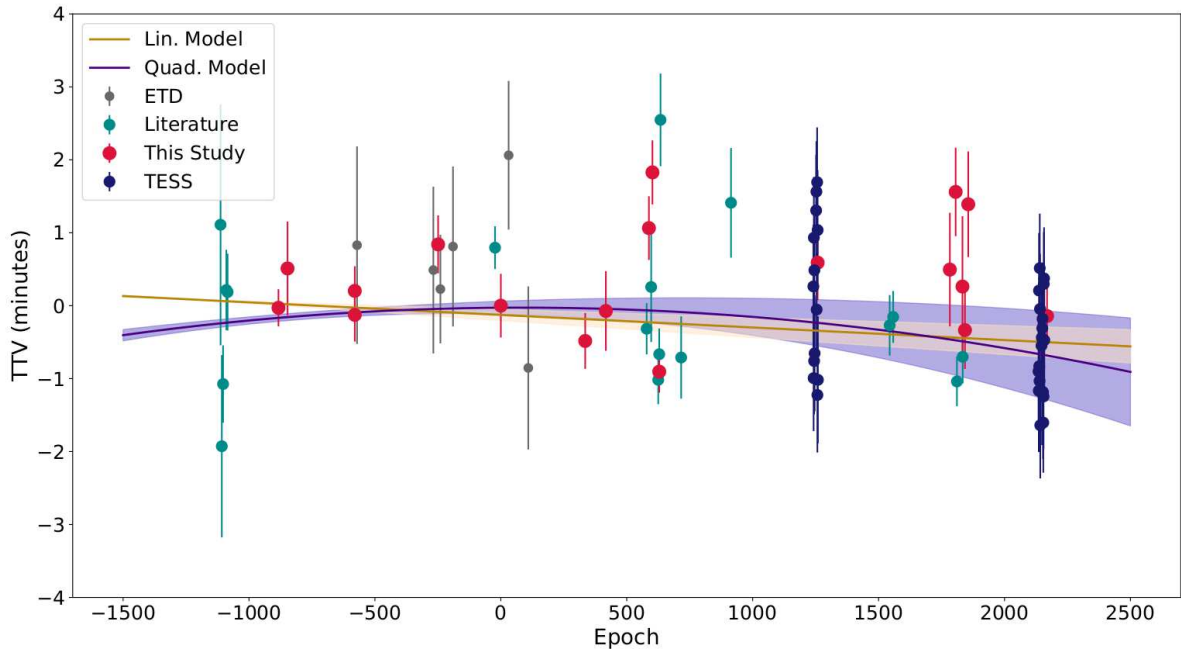
Figure 6. TTV diagram of KELT-1 b with linear (in orange) and quadratic models (purple) superimposed on data together with their uncertainties in shades with the same colours as the models.

We then continued our analysis with the residuals of the O-C values from the linear model to search for potential periodic signals in the data, which would hint at the existence of gravitationally bound perturbers. We obtained a Lomb-Scargle periodogram of the residuals with the help of a Python code based on the TIMESERIES function of the ASTROPY package (VanderPlas 2018). We did not find any statistically significant peak down to a 20% false alarm probability (FAP) level based on mid-transit timing data from 72 light curves unevenly distributed over ∼ 10.9 years with a mean error of 41 ± 16 s. Therefore we find no evidence for a significant periodicity in the TTV diagram. We followed the same analysis approach by making use of the published measurements of mid-transit timings instead of our own values, but the scatter on the O-C diagram increased and the goodness-of-fit statistics decreased significantly. This occurred despite more than two thirds (50 of 72) of the data points being our own measurements from our observations and the TESS light curves. Therefore, we continued our analysis based on the transit times we calculated in a homogeneous way.

We experimented by making use of 49 points within 1σ of the average error bar of mid-transit timing measurements. This eliminated all the ETD data, ten light curves from the literature (including the first two light curves from Siverd et al. 2012), and eight of our own light curves. The linear model was again found to be better than the quadratic model, and there was no significant peak in the frequency analysis. Therefore, the selection of data based on the size of the error bars did not bring any improvement except for the appearance of a candidate frequency at ∼ 283 days with 1.9% FAP, which we note for future reference.

We then used the β-factor as an elimination criterion to work with the light curves least affected by correlated noise ($\beta < 2.5$). While all ETD and literature light curves passed this criterion, ten TESS

transits were eliminated of which seven were from sector 17. The total scatter of the mid-transit timings from this sector is slightly larger (2.95 min compared to 2.12 min for sector 57) as observed from the TTV diagram in Fig. 6. Therefore, we find the scatter in the TTV diagram, in excess of that implied by observational uncertainties, to be attributable to potential activity-induced spot-crossing events during transits. Spot-induced asymmetries in some of the light curves are just about noticeable. However, they are not persistent from one transit light curve to another so we cannot use them to track and recover a rotation period. The ground-based light curves, on the other hand, are heavily influenced by white noise, which dominates the red noise. When we analyze only the light curves with PNR values less than 2.0 (61 in total), all 32 TESS light curves survive. However, this choice brings no improvement to the results either. After all these experiments, we decided to present our results based on the entire data set, which we provided as online material.

4 CONCLUSIONS

KELT-1 b was one of only seven transiting BDs ($13\,M_{Jup} < M_p < 80\,M_{Jup}$) known at the time it was discovered (Siverd et al. 2012). In the intervening ten years, this number has increased to 24 (as reported in the TEPCat[3] catalogue; Southworth 2011). This is due to the mechanisms of their formation and migration and is despite the biases brought by the transit method, which favours the detection of large objects at short orbital periods. The recently-discovered objects GPX-1 b (Benni et al. 2021), TOI-263 b (Palle et al. 2021), and TOI-519 b

---

[3] https://www.astro.keele.ac.uk/jkt/tepcat/
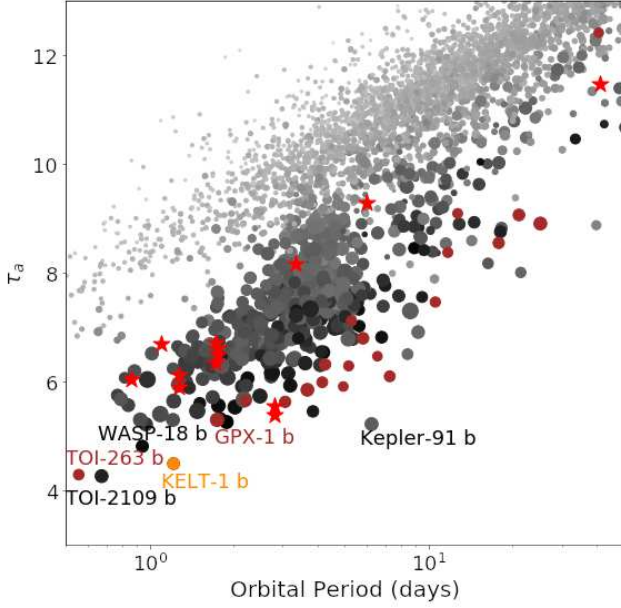
Figure 7. Plot of the τ_a parameter, which is proportional to the e-folding timescale of orbital decay, with respect to the orbital period for planets, close-in brown dwarfs and some low-mass stars in binary systems. The sizes of the data points depend on the radii of the objects (larger points for larger objects) and their colours depend on their masses (darker grey for more massive objects). BD-mass objects are in brown, also scaled with their radii, and low-mass stars are given with red stars while KELT-1 is in orange based on the parameters derived within this study, the error bars of which are smaller than the size of the marker.

(Parviainen et al. 2021) are other examples of BD-mass objects on short-period orbits. Considering the paucity of such massive objects in the close vicinity of their host stars (the "brown dwarf desert"), it is reasonable to expect their orbits to decay under strong tidal interactions with their host stars. In fact, KELT-1 b is one of the strongest candidates for orbital decay based on its e-folding timescale, which is proportional to the quantity

$$\tau_a = \frac{M_\star}{M_p} \left(\frac{a}{R_\star} \right)^5 \tag{5}$$

as defined by Siverd et al. (2012). We plot this dimensionless quantity versus orbital period in Fig. 7 and label some interesting objects together with KELT-1 b. Planet data (grey circles) are based on relevant parameter values for NASA Exoplanet Archive[4] composite data set, while that for BDs (brown circles) are from TEPCat. We also included 14 low-mass stellar companions with orbital periods smaller than 100 d and less massive than 0.25 $M_\odot$ (red stars) from the Detached Eclipsing Binary Catalogue (DEBCat)[5] (Southworth 2015). KELT-1 b's location is based on the parameters derived within this study. The so-called sub-Jovian desert is visible as the relatively empty triangular area roughly between $\tau_a \sim 10^7$ and $\tau_a \sim 10^8$ below an orbital period of 2.5 d (Baştürk et al. 2020).

Although KELT-1 b stands out as one of the most promising candidates for period decay, planetary mass and orbital period are not the only factors determining the stability of planet's orbit. Despite being the only case for which orbital decay has been detected convincingly,
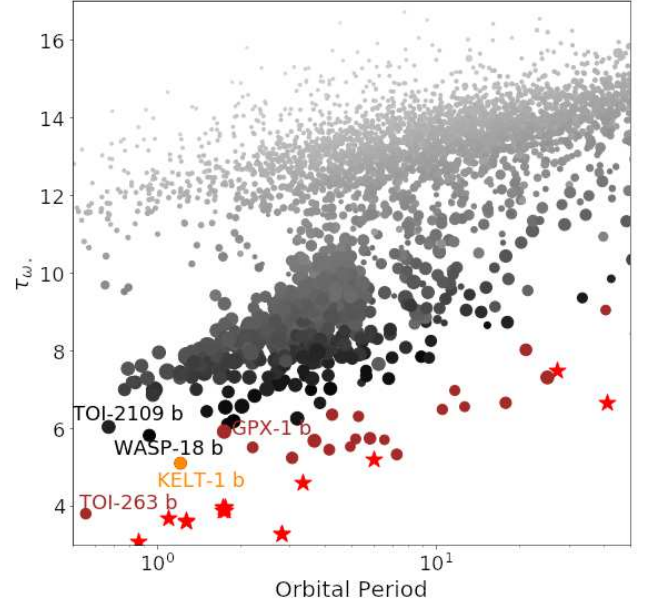
Figure 8. Plot of the $\tau_{\omega_\star}$ parameter, which is proportional to the synchronization timescale of the stellar spin with the orbital period, versus the orbital period of the companions. Point sizes and colour scale are the same as in Fig. 7.

WASP-12 b does not stand out on this plot. Nevertheless, it has a relatively lower τ_a value of $\sim 10^{5.4}$.

Another dimensionless quantity defined by Siverd et al. (2012) as

$$\tau_{\omega_\star} = \left(\frac{M_\star}{M_p} \right)^2 \left(\frac{a}{R_\star} \right)^3 \tag{6}$$

is proportional to the synchronization timescale of the stellar spin with the orbital period. KELT-1 b should have the shortest synchronization timescale based on its location on this plot (Fig. 8). Tidal interactions with the planet spin up the host star and a stable tidal equilibrium can be achieved when the total angular momentum is sufficient (Ogilvie 2014). However, for the mid-F star hosting KELT-1 b, the dissipation mechanism is unclear because it should have a shallow convective zone.

Based on our analysis of timing data spanning almost eleven years of observations, we find no evidence for decay in the orbit of KELT-1 b because the linear-ephemeris model turned out to be superior to the quadratic model. Thus, we constrained a lower limit for the tidal quality parameter as $Q'_\star > (8.5 \pm 3.9) \times 10^6$. Considering that the host star is relatively hot ($T_{\mathrm{eff}} \sim 6471$ K) and therefore should have a thin convective envelope, the tidal energy it should dissipate in one revolution of the planet in its tidal bulge should even be lower than that predicted by the canonical value for stars with convective envelopes. The characteristic timescale for orbital decay (τ_{decay}) is not more than 140 Myr (95% confidence) as well. However, we find an age of $1.65^{+0.89}_{-0.65}$ Gyr from isochrone fitting. We interpret these results as indicators of a tidal equilibrium in the system. Our interpretation is further supported by the proximity of the rotation periods found both from the projected rotational velocity from spectral line broadening (1.33 d, Siverd et al. 2012) and spot-induced modulation from the frequency spectrum (1.52 d, von Essen et al. 2021) to the orbital period (1.21 d, this study) despite the large uncertainty on the rotational period.

Although tidal equilibrium is likely, the mechanism causing the angular momentum transfer so that the total angular momentum is

sufficient for the equilibrium is unclear. Nevertheless, other similarly short-period and massive objects have been found orbiting relatively hotter stars than the Sun with thinner convective envelopes as KELT-1. In fact, more massive companions are suggested to be hosted by hotter stars on average (Jiang et al. 2021). This is most probably the consequence of a more massive protoplanetary disk that would form around a larger star to support the formation of more massive planets in turn (Andrews et al. 2013). This mass-mass correlation agrees with the predictions of the in situ formation mechanism (Armitage 2018). Then such massive planets and BDs may have formed closer to their stars by accreting material from a massive protoplanetary disk and then migrated inwards even further by interacting with it or through Kozai-Lidov oscillations and then stabilized on short-period orbits after a tidal equilibrium is achieved. After all, we still do not know either the maximum mass of the object that can be formed by accretion in a disk or the minimum mass formed by disk instability. Therefore, a classification based on its formation mechanism as a planet via core-accretion or as a BD via disk-instability is a matter of debate. Our results show that KELT-1 b is similar to other massive planets in terms of its orbital properties. However, our global model of the available light curves (including that of TESS) and RV data with a full-phase coverage suggests an orbital eccentricity, with a significance of $\sim 1.5\sigma$, as has been noticed in earlier work (Beatty et al. 2014; von Essen et al. 2021). Since the circularization timescale is very short, a potential third body on a larger orbit can explain the small but a non-zero eccentricity if it is real, which requires more and precise follow-up transit and occultation observations of the target. They will also help us further constrain the tidal quality parameter of its host star and understand the extent of tidal interactions in this important system.

ACKNOWLEDGEMENTS

DATA AVAILABILITY

Some of the light curves to derive mid-transit times were downloaded from Exoplanet Transit Database at http://var2.astro.cz/ETD/. All other light curves appearing for the first time in this article are presented as online material. Mid-transit times derived from our own light curves as well as that of other observers' and TESS light curves are presented as online data sets too through Vizier Online.

REFERENCES

Andrews S. M., Rosenfeld K. A., Kraus A. L., Wilner D. J., 2013, ApJ, 771, 129
Armitage P. J., 2018, in Deeg H. J., Belmonte J. A., eds, , Handbook of Exoplanets. p. 135, doi:10.1007/978-3-319-55333-7_135
Astropy Collaboration et al., 2013, A&A, 558, A33
Astropy Collaboration et al., 2018, AJ, 156, 123
Baştürk Ö., Yalçınkaya S., Esmer E. M., Tanrıverdi T., Mancini L., Daylan T., Southworth J., Keten B., 2020, MNRAS, 496, 4174
Baluev R. V., et al., 2015, MNRAS, 450, 3101
Barker A. J., Ogilvie G. I., 2009, MNRAS, 395, 2268
Beatty T. G., et al., 2014, ApJ, 783, 112
Beatty T. G., Madhusudhan N., Pogge R., Chung S. M., Bierlya A., Gaudi B. S., Latham D. W., 2017, AJ, 154, 242
Benni P., et al., 2021, MNRAS, 505, 4956
Bianchi L., Shiao B., Thilker D., 2017, ApJS, 230, 24
Birkby J. L., et al., 2014, MNRAS, 440, 1470
Brandeker A., Cataldi G., 2019, A&A, 621, A86
Choi J., Dotter A., Conroy C., Cantiello M., Paxton B., Johnson B. D., 2016, ApJ, 823, 102
Claret A., Bloemen S., 2011, A&A, 529, A75
Collins K. A., Kielkopf J. F., Stassun K. G., Hessman F. V., 2017, AJ, 153, 77
Cutri R. M., et al., 2003, VizieR Online Data Catalog, p. II/246
Cutri R. M., et al., 2021, VizieR Online Data Catalog, p. II/328
Eastman J., 2017, EXOFASTv2: Generalized publication-quality exoplanet modeling code (ascl:1710.003)
Eastman J., Gaudi B. S., Agol E., 2013, PASP, 125, 83
Eastman J. D., et al., 2019, arXiv e-prints, p. arXiv:1907.09480
Fulton B. J., Shporer A., Winn J. N., Holman M. J., Pál A., Gazak J. Z., 2011, AJ, 142, 84
Gaia Collaboration et al., 2016, A&A, 595, A1
Gaia Collaboration et al., 2021a, A&A, 649, A1
Gaia Collaboration et al., 2021b, A&A, 649, A6
Grether D., Lineweaver C. H., 2006, ApJ, 640, 1051
Henden A. A., Templeton M., Terrell D., Smith T. C., Levine S., Welch D., 2016, VizieR Online Data Catalog, p. II/336
Høg E., et al., 2000, A&A, 355, L27
Jenkins J. M., et al., 2016, in Proc. SPIE. p. 99133E
Jiang J., Zhao D., Ji X., Xie B., Fahy K. A., 2021, Universe, 7, 88
Lindegren L., et al., 2021, A&A, 649, A4
Maciejewski G., et al., 2018, Acta Astron., 68, 371
Maciejewski G., et al., 2022, arXiv e-prints, p. arXiv:2209.10597
Mugrauer M., Zander J., Michel K.-U., 2022, Astronomische Nachrichten, 343, e24017
Ogilvie G. I., 2014, ARA&A, 52, 171

Palle E., et al., 2021, A&A, 650, A55

Parviainen H., et al., 2021, A&A, 645, A16

Ricker G. R., et al., 2015, Journal of Astronomical Telescopes, Instruments, and Systems, 1, 014003

Salvatier J., Wieckiâ T. V., Fonnesbeck C., 2016, PyMC3: Python probabilistic programming framework, Astrophysics Source Code Library, record ascl:1610.016 (ascl:1610.016)

Schlegel D. J., Finkbeiner D. P., Davis M., 1998, ApJ, 500, 525

Siverd R. J., et al., 2012, ApJ, 761, 123

Southworth J., 2011, MNRAS, 417, 2166

Southworth J., 2015, in Rucinski S. M., Torres G., Zejda M., eds, Astronomical Society of the Pacific Conference Series Vol. 496, Living Together: Planets, Host Stars and Binaries. p. 164 (arXiv:1411.1219)

Southworth J., et al., 2009, MNRAS, 396, 1023

Southworth J., et al., 2014, MNRAS, 444, 776

Southworth J., Bohn A. J., Kenworthy M. A., Ginski C., Mancini L., 2020, A&A, 635, A74

Spiegel D. S., Burrows A., Milsom J. A., 2011, ApJ, 727, 57

Tayar J., Claytor Z. R., Huber D., van Saders J., 2020, arXiv e-prints, p. arXiv:2012.07957

Torres G., Andersen J., Giménez A., 2010, A&ARv, 18, 67

VanderPlas J. T., 2018, ApJS, 236, 16

Winn J. N., et al., 2008, ApJ, 683, 1076

Yalçınkaya S., et al., 2021, Acta Astron., 71, 223

von Essen C., et al., 2021, A&A, 648, A71

This paper has been typeset from a TEX/LATEX file prepared by the author.